NANOMATERIALS

Self-assembly of nanocrystals into strongly electronically coupled all-inorganic supercrystals

Igor Coropceanu[1]†, Eric M. Janke[1]†, Joshua Portner[1]†, Danny Haubold[1,2], Trung Dac Nguyen[3], Avishek Das[4], Christian P. N. Tanner[4], James K. Utterback[4], Samuel W. Teitelbaum[5], Margaret H. Hudson[1], Nivedina A. Sarma[1], Alex M. Hinkle[1], Christopher J. Tassone[6], Alexander Eychmüller[2], David T. Limmer[4,7,8], Monica Olvera de la Cruz[3,9], Naomi S. Ginsberg[4,8,10,11], Dmitri V. Talapin[1,12]*

Colloidal nanocrystals of metals, semiconductors, and other functional materials can self-assemble into long-range ordered crystalline and quasicrystalline phases, but insulating organic surface ligands prevent the development of collective electronic states in ordered nanocrystal assemblies. We reversibly self-assembled colloidal nanocrystals of gold, platinum, nickel, lead sulfide, and lead selenide with conductive inorganic ligands into supercrystals exhibiting optical and electronic properties consistent with strong electronic coupling between the constituent nanocrystals. The phase behavior of charge-stabilized nanocrystals can be rationalized and navigated with phase diagrams computed for particles interacting through short-range attractive potentials. By finely tuning interparticle interactions, the assembly was directed either through one-step nucleation or nonclassical two-step nucleation pathways. In the latter case, the nucleation was preceded by the formation of two metastable colloidal fluids.

Self-assembly of nanocrystals (NCs) into long-range ordered arrays can enable bottom-up design of hierarchically organized functional and multifunctional materials (*1*, *2*). A large body of work has identified conditions for the assembly of colloidal NCs into face-centered cubic (fcc) and body-centered cubic (bcc) solids (*3*, *4*), multicomponent binary and ternary NC superlattices (*5*–*8*), and quasicrystalline structures (*9*, *10*). These approaches used NCs with surfaces functionalized by long hydrocarbon chains or surface-tethered DNA strands that supported colloidal stability but also separated NCs with electrically insulating barriers at least 1 to 2 nm in thickness (fig. S1). These barriers lead to poor electronic conductivity of ordered NC assemblies and constrain their prospects for practical applications. Some collective effects can develop through distant coupling of plasmonic excitations (*11*) or magnetic dipoles (*12*), but free electron movement is needed to develop conduction bands. The combination of translational symmetry and strong electronic coupling holds the promise of enabling a general platform for the construction of new functional materials from the available library of NCs.

Strong coupling between NCs can be achieved by using very compact (typically inorganic) surface ligands. For example, thin films of CdSe NCs capped with $In_2Se_4^{2-}$ surface ligands can develop band-like electronic transport (*13*). These ligands add charge to the NC surface, and NCs act as electrostatically stabilized colloids in polar solvents. However, NCs with such ligands fail to form ordered superstructures because the van der Waals attractive forces arising between touching NCs are too strong and arrest the system as a gel or glass (*14*). An alternative approach to building strongly electronically coupled NC solids is to remove the native insulating organic ligands after assembly (*15*, *16*), which sometimes results in the oriented attachment of NCs (*16*–*18*). However, irreversible oriented attachment cannot produce large, ordered supercrystalline (SC) domains because structural defects accumulate. This problem is inherent to any assembly process that lacks a self-healing pathway enabled by microreversibility (*19*, *20*).

We describe a new class of all-inorganic SC materials that combine long-range order with strong electronic coupling. As building blocks, we used NCs (metals such as Au, Pt, and Ni or semiconductors such as PbS and PbSe) capped with small and conductive metal chalcogenide complex (MCC) ligands (such as $Sn_2S_6^{4-}$, $Sn_2Se_6^{4-}$, $In_2Se_4^{2-}$, AsS_4^{3-}, and $Cu_6S_4^{2-}$) that we have previously described (*21*). Through controlled flocculation using multivalent salts, these NCs assembled into fcc and hexagonal close-packed SCs, as well as other structures with more complex symmetry (Fig. 1 and figs. S2 and S3). Alkali metals, NH_4^+, or $N_2H_5^+$ served as cations for charge balance.

Faceted three-dimensional SCs of 5-nm Au NCs capped by $Sn_2S_6^{4-}$ ions (Fig. 1, A and B) showed micrometer-size domains containing ~10^8 NCs. The MCC ions remained in the superlattice (fig. S4) and separated the Au NCs by ~0.3 nm (fig. S5). The small- and wide-angle x-ray scattering (SAXS and WAXS, respectively) patterns of macroscopic samples showed two sets of fcc reflections: from the atomic planes inside individual NCs at the momentum transfers $q > 1$ Å^{-1} and from the SC planes at $q < 1$ Å^{-1} (Fig. 1, C and D). These structures formed spontaneously upon addition of $K_4Sn_2S_6$ to a concentrated (~100 mg/ml) colloidal solution of Au NCs with $Sn_2S_6^{4-}$ surface ligands in polar solvents *N*-methylformamide (NMF) or hydrazine (see supplementary materials section 1). The addition of 1:1 electrolytes such as NaCl precipitated amorphous aggregates (fig. S6) typical for irreversible binding of NCs, as had been seen with many previous studies of electrostatically stabilized NC colloids (*14*). An additional observation was that NCs of materials with high dielectric constant (ε_{NC}) such as metals ($\varepsilon_{NC} \to \infty$), PbS ($\varepsilon_{NC} = 170$), and PbSe ($\varepsilon_{NC} = 220$) readily formed SCs, whereas any NCs with $\varepsilon_{NC} < 20$ (CdSe, InAs, and Fe_2O_3) formed gels or glasses (figs. S7 to S21).

These observations suggest possible connections among SC formation, ionic charge, and ε_{NC}. An understanding of the phase behavior (formation of SCs versus disordered glass or gel structures) begins with the knowledge of the interaction potentials between particles. However, the exact form of pair potentials for colloidal NCs <10 nm is generally not known and cannot be easily extracted from available experimental data (*22*). Derjaguin-Landau-Verwey-Overbeek (DLVO) theory (*23*) can serve as the minimal framework accounting for three major components: van der Waals (vdW) attraction, electrostatic repulsion, and an additional steep short-range repulsion at hard contact of NC cores (see supplementary materials section 2.1). For a broad range of input parameters, such as surface charge and Hamaker constant, the competition between vdW attraction and electrostatic repulsion results in a narrow (<1 nm width) potential well with depth larger than 5 k_BT, where k_B is the Boltzmann constant and T is temperature (Fig. 2A).

Computational studies on model colloids have shown that it is not only the depth but also the range of pair potentials that plays a critical role in the formation of crystalline phases versus glasses or gels (*24*, *25*). As a rule, attractive potentials with a range of <20% of the particle diameter and a depth of 3 to 4 k_BT are most favorable for crystal nucleation and

[1]Department of Chemistry, James Franck Institute, and Pritzker School of Molecular Engineering, University of Chicago, Chicago, IL 60637, USA. [2]Physical Chemistry, Technische Universität Dresden, Dresden, Germany. [3]Department of Chemical and Biological Engineering, Northwestern University, Evanston, IL 60208, USA. [4]Department of Chemistry, University of California, Berkeley, CA 94720, USA. [5]Department of Physics and Beus CXFEL Labs, Biodesign Institute, Arizona State University, Tempe, AZ 85287, USA. [6]Stanford Synchrotron Radiation Lightsource, SLAC National Accelerator Laboratory, Menlo Park, CA 94025, USA. [7]Chemical Sciences Division and Materials Sciences Division, Lawrence Berkeley National Laboratory, Berkeley, CA 94720, USA. [8]Kavli Energy NanoSciences Institute, University of California, Berkeley, CA 94720, USA. [9]Department of Materials Science and Engineering, Department of Chemistry, and Department of Physics and Astronomy, Northwestern University, Evanston, IL 60208, USA. [10]Department of Physics, University of California, Berkeley, CA 94720, USA. [11]Materials Sciences Division, Molecular Biophysics and Integrated Bioimaging Division, Lawrence Berkeley National Laboratory, Berkeley, CA 94720, USA. [12]Center for Nanoscale Materials, Argonne National Laboratory, Argonne, IL 60517, USA.
*Corresponding author. Email: dvtalapin@uchicago.edu
†These authors contributed equally to this work.

growth, whereas the exact shape of the potential is less important (*25*, *26*). For a 5-nm-diameter Au NC, this would correspond to an extremely short, subnanometer range of attraction. At this length scale, continuum theories such as DLVO can provide only approximate guidance (*27*), whereas accurate atomistic simulations are impeded by the large size of the system.

According to the Noro-Frenkel extended law of corresponding states, the equilibrium phase diagram of different systems with short-range attraction can be represented by particles interacting in square-well potentials (Fig. 2C, inset) with depth u_0 and width $2\lambda R$, where R is the particle radius (*26*). For $\lambda < 0.2$, regardless of the exact well shape, the phase diagram consists of two equilibrium phases, a colloidal fluid and a solid, with a "hidden" binodal curve separating two metastable fluid phases (Fig. 2B) (*24*, *28*). Haxton *et al.* modeled the dynamics of a colloidal fluid as function of u_0 and λ (Fig. 2C) and mapped regions with high probability to form crystals (regions I and II), metastable fluids with a prohibitively slow nucleation rate (region III), kinetically frozen metastable gels (region IV), and a stable liquid phase (region V).

Although the exact parameters of NC pair potentials may be difficult to access, the appearance, evolution, and final state of NC colloid offer insights into its location within the phase diagram. In our experiments, the formation of SCs was often preceded by separation of NC colloid into dense and dilute fluid phases (Fig. 3A; see supplementary materials section 2.2). Such behavior was reported for polymethylmethacrylate (PMMA) spheres (*29*) and globular proteins (*30*) but not for inorganic NCs. For Au NCs, optical studies showed that the dense fluid was highly metastable and converted into SCs within seconds, but for PbS NCs, the dilute and dense fluid phases, both with no long-range order, could coexist for many hours, followed by the slow formation of fcc SCs from the dense fluid phase. The dense fluid phase exhibited a short-range structure factor (fig. S22) resulting from interparticle correlations at high concentration, similar to previous reports of large PMMA spheres (*31*). Such triple-phase coexistence of two metastable colloidal fluids and SCs confirmed the presence of a fluid-fluid binodal curve and further supported that our charge-stabilized NC colloids followed the predictions for spheres with short-range attractive potentials.

The formation of SCs required the use of multivalent anionic ligands on the NC surface and as a flocculant (co-ions) to induce self-assembly. By contrast, the addition of NaCl or another 1:1 electrolyte resulted in gelation for all studied conditions, which is characteristic of region III shown in Fig. 2C and also agrees with the potentials shown in Fig. 2A,

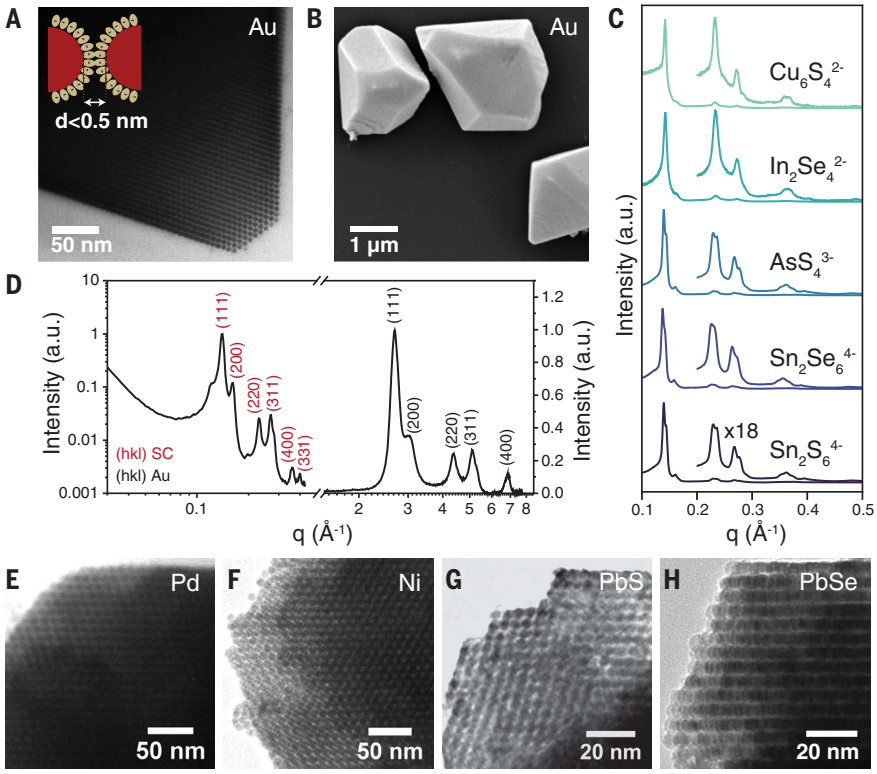

Fig. 1. Compositional diversity of all-inorganic NC assemblies. (**A**) TEM and (**B**) scanning electron microscopy (SEM) images of supercrystals assembled from 3.8-nm Au NCs with $(N_2H_5)_4Sn_2S_6$ surface ligands. (**C**) SAXS patterns for self-assembly of a population of 5-nm Au NCs with different MCC ligands, yielding crystalline superlattices in each case. Inset: vertically magnified view of the SAXS pattern after the 111 peak. (**D**) SAXS and WAXS patterns of supercrystals assembled from Au NCs with $(N_2H_5)_4Sn_2S_6$ ligands showing fcc crystalline order at both the supercrystal and atomic length scales. Data have been normalized to the 111 peaks. (**E** to **H**) TEM micrographs of different all-inorganic NC assemblies showing ordered domains of 9 nm Pd, 9 nm Ni, 5 nm PbS, and 6 nm PbSe NCs with MCC ligands, respectively.

the attractive well of ~6 k_BT being too deep for reversible binding and crystallization at experimentally accessible time scales (*25*, *32*). Multivalent counterions can also promote the crystallization of NCs in polar solvents (*33*). The observation that NC assembly required the addition of a salt containing multivalent ions could not be explained by DLVO. Generally, concentrated and multivalent electrolytes showed strong ion-ion correlations. Ion correlations under confinement resulted in an additional attractive force (*34*), but for the multivalent co-ions used in this study, the effect was small (*35*). However, we show here that co-ion valency can have a prevalent effect on the effective two-body potentials for NCs with high polarizability and correspondingly large ε_{NC}.

Our molecular dynamics (MD) simulations, as well as direct chemical analysis data (fig. S23), showed that multivalent ions formed a dense layer near the NC surface for metallic NCs ($\varepsilon_{NC} \to \infty$), whereas typical dielectric NCs ($\varepsilon_{NC} < 20$) had only loosely associated counterions with the NC surface (Fig. 2D). The radial density profiles of the anions revealed that as ε_{NC} increased, the anions accumulated near the NC surface beyond one full monolayer (fig. S24). The driving force resulted from the dielectric mismatch between the NCs and the surrounding medium (*36*). This mismatch induced polarization, which created an attraction between the anions and the image charges inside the NCs (*37*). As the anion valency was decreased, the surface-induced charges were reduced, which led to loose packing of the condensed anions (fig. S25).

MD simulations of two NCs surrounded by multivalent anions revealed an additional force exerted on each NC as a function of their center-to-center distance (see supplementary materials section 2.3). This force was purely repulsive at short range (Fig. 2E), reduced the depth of the attractive well, and enabled the microreversibility of NC binding necessary for nucleation and growth of long-range ordered SCs. Our simulation of NC colloids further corroborated this hypothesis, showing that when the attractive well was deep (~6 k_BT), the particles were arrested into gel-like structures, similar to experimentally observed structures for NCs with $\varepsilon_{NC} < 20$. However, when the

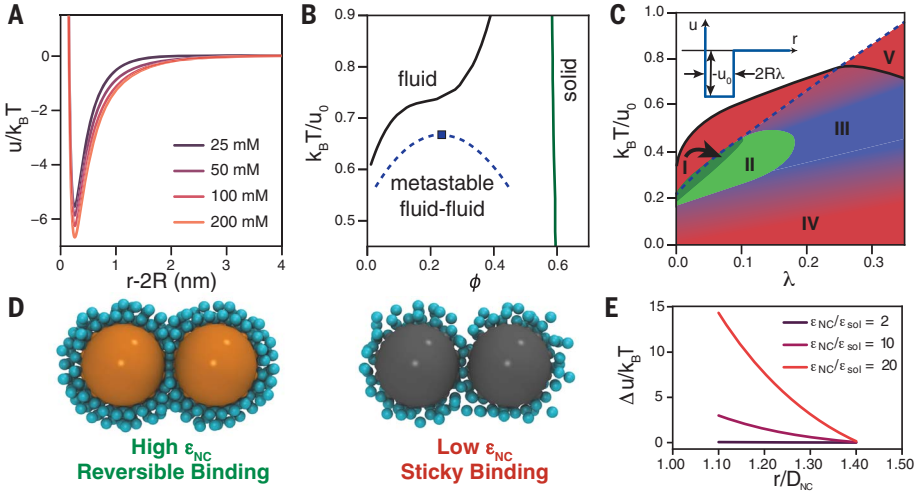

Fig. 2. Modeling interactions and phase equilibria of charge-stabilized colloidal nanocrystals. (**A**) Estimated pair potential for 4.5-nm Au NCs in the presence of different concentrations of 1:3 electrolyte. (**B**) Phase diagram for a colloid with a square-well attractive potential with λ = 0.18. Solid square shows the metastable fluid-fluid critical point. Data were taken from references (*25*) and (*28*). (**C**) Probability of supercrystal nucleation represented by color gradients (green indicates high; blue, intermediate; and red, low) as a function of u_0 and λ of a square-well potential for a colloid with volume fraction of ϕ = 0.1. The diagram highlights regions corresponding to (I) one-step nucleation, (II) two-step nucleation, (III) coexistence of two metastable fluids with a slow nucleation rate, (IV) gel formation, and (V) a thermodynamically stable colloidal fluid. The dashed blue curve is the metastable fluid-fluid binodal curve, and the solid black curve is the thermodynamic boundary for stability of an fcc crystal. Inset: a square-well potential determined by the depth (u_0) and range of the attraction (λ). Data were taken from reference (*25*). (**D**) Qualitative difference in interactions of NCs with high (ε_{NC} = 200) and low (ε_{NC} = 10) dielectric constant, with multivalent ions resulting in reversible and sticky NC binding, respectively. (**E**) Computed repulsive component of the interparticle potential at varying dielectric contrast $\varepsilon_{NC}/\varepsilon_{sol}$, where ε_{sol} is solvent dielectric constant. The repulsive interaction increases for NCs with high polarizability.

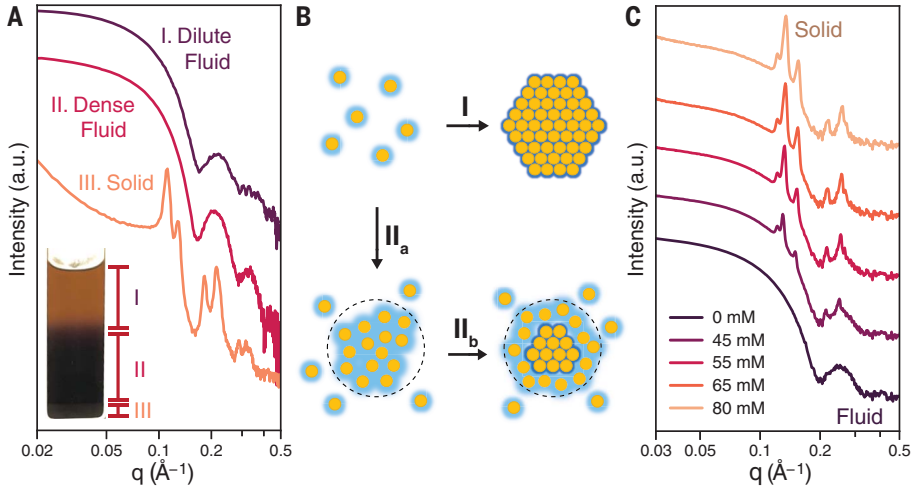

Fig. 3. Triple-phase coexistence and nucleation in charge-stabilized NC colloids. (**A**) Homogeneous colloidal solutions of 5.5-nm PbS NCs capped with $Sn_2S_6^{4-}$ ligands in NMF spontaneously form three phases upon addition of acetonitrile. SAXS data show three separate phases of dilute fluid, dense fluid, and fcc solid supercrystals. Inset: photograph of 5.5-nm PbS NC colloid showing the coexistence of three phases. (**B**) Schematic representation of one-step nucleation (I) and two-step nucleation (II_a and II_b) of supercrystals; phase separation precedes crystallization in the latter case. (**C**) In situ SAXS data for one-step nucleation of 4.6-nm Au NCs capped with $(N_2H_5)_4Sn_2S_6$ and flocculated by gently increasing the $(N_2H_5)_4Sn_2S_6$ concentration.

attraction strength was moderate (~3 to 4 k_BT), the coexistence of a metastable high-density liquid and crystal was present (fig. S26), closely resembling the behavior of metal semiconductor NCs with large ε_{NC}.

The metastable binodal curve in the colloidal phase diagram includes a fluid-fluid critical point (Fig. 2B). ten Wolde and Frenkel suggested that critical density fluctuations in the vicinity of this critical point lower the activation barrier for crystal nucleation (*24*). The SC nucleation can proceed along two different pathways (Figs. 2C, regions I and II, and 3B) (*24*, *25*). In a narrow window of parameters very close to the binodal curve, classical one-step nucleation (region I) is predicted to be the main pathway to a crystalline state. Indeed, in situ SAXS studies showed that a gentle increase of $(N_2H_5)_4Sn_2S_6$ concentration in hydrazine up to ~50 mM induced a rapid nucleation of 4.6 nm Au NCs into SCs, which grew at the expense of the free colloid (Fig. 3C and fig. S27).

A qualitatively different pathway was observed after the rapid addition of 100 to 125 mM $(N_2H_5)_4Sn_2S_6$ to a colloid of similarly sized Au NCs. Instead of direct nucleation of SCs, the colloidal solution divided into two fractions with different density (figs. S28 and S29). The dense phase initially showed no long-range order and resembled aggregated NCs but ultimately converted into SCs. This showed that the dense phase was not an arrested state but rather a dynamically evolving intermediate preceding SC formation, with transmission electron microscopy (TEM) studies further suggesting that crystallization occurs within the matrix of disordered NCs (figs. S30 to S33). In the case of 5.5-nm PbS NCs in NMF flocculated with K_3AsS_4 in the presence of acetonitrile (Fig. 3A and fig. S34), SC nucleation was preceded by a separation of the homogeneous colloid into droplets of dilute and dense fluids according to the binodal separation of two fluids in Fig. 2B, and the nucleation occurred within the metastable dense fluid phase. Such a pathway is reminiscent of the nonclassical two-step nucleation, which is rather common for globular proteins (*38*, *39*).

In many previous studies, NC films with strong electronic coupling and high electron mobility showed no long-range order, whereas long-range-ordered two- and three-dimensional SCs typically used insulating organic ligands. The resulting "order versus coupling" tradeoff (Fig. 4A; see supplementary materials section 2.4) is detrimental for the applications of colloidal NCs in optoelectronic devices. For the all-inorganic SCs described in this work, compared with SCs with traditional organic surfactants, the smaller interparticle spacing in all-inorganic SCs and the semiconducting nature of MCC ligands enabled much stronger electronic coupling between neighboring NCs while

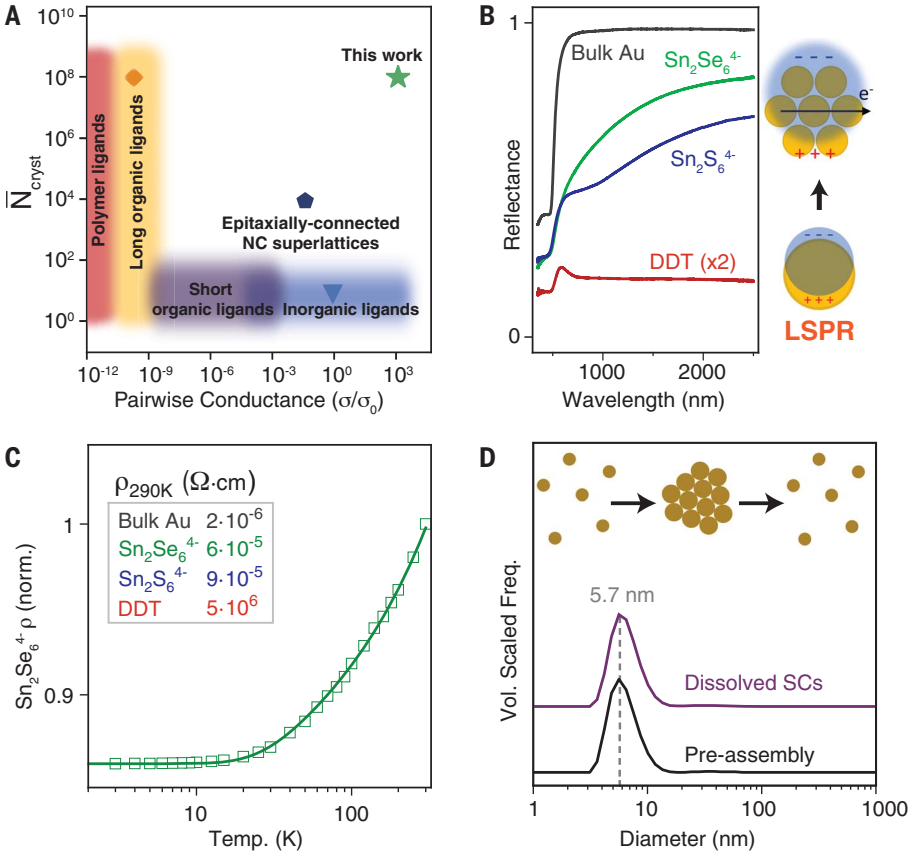

Fig. 4. Strong coupling and reversibility in all-inorganic NC superlattices. (**A**) Order-coupling diagram for existing NC solids. As a measure of electronic coupling in different ordered and disordered structures, we used the interparticle conductance ($\sigma^* = \sigma/\sigma_0$) normalized by the conductance quantum ($\sigma_0 = 2e^2/h$), where e is the electron charge and h is Plank's constant. As a measure of the ordering, we took the average number of particles in a crystalline domain. The data points indicated are as follows: red diamond, superlattices of DDT-capped Ag NCs (*47*); light blue inverted triangle, film of inorganically capped HgTe NCs (*48*); and dark blue pentagon, epitaxially connected PbSe superlattice by oriented attachment (*17*). Green star indicates data from the present work. (**B**) Left: reflectance data of 5-nm Au NCs capped with MCC and DDT ligands compared with bulk Au. Right: schematic for delocalization of LSPR in strongly coupled NC arrays. (**C**) Temperature-dependent resistivity data for supercrystals assembled from 5-nm Au NCs with $Sn_2Se_6^{4-}$ ligands. Inset: ρ at 290 K for bulk Au and Au NCs with three different ligands. (**D**) Dynamic light-scattering data showing that colloidal NCs can be assembled into SCs and then redissolved to recover the original colloidal solution.

maintaining the high NC order and low strain previously observed only for SCs containing soft, deformable organic ligands (fig. S35).

The optical reflectance spectra measured for Au SCs with different surface ligands showed the crossing from weakly coupled localized surface plasmon resonance (LSPR) in the arrays of Au NCs with 1-dodecanethiol (DDT) ligands into the strong coupling regime for SCs assembled from Au NCs with $Sn_2S_6^{4-}$ ions approaching that of bulk metals (Fig. 4B and fig. S36). For Au NCs assembled with more conductive and polarizable $Sn_2Se_6^{4-}$ ions, the transition to metallic reflectance was even more complete, with higher reflectance overall and no sign of a residual LSPR component.

Measurements of direct current transport further supported assignment of metallic character to Au NC solids with MCC ligands (Fig. 4C). Resistivity decreased monotonically from 300 down to 3 K with no evidence of thermally activated transport between localized states that would manifest as increasing resistivity in the low-temperature limit. Instead, the temperature-dependent resistivity data were well described by the Boltzmann transport theory, as for typical metallic solids. A Bloch–Grüneisen model fit (*40*) successfully captures the phenomenology of the R versus T relation and is plotted as a solid line through the discrete data points (fig. S37). Between 300 and 3 K, the resistivity of the sample dropped by a factor of 0.86, yielding a residual resistivity ratio (RRR) $\rho_{300K}/\rho_{4K} = 1.16$. Such values of RRR are commonly measured from metallic alloys (*41*, *42*) and degenerately doped crystalline semiconductors (*43*). Magnitudes of 290 K resistivities (Fig. 4C, inset) of $Sn_2Se_6^{4-}$-capped Au solids without any thermal annealing are within a factor of 30 of evaporated bulk Au films (Fig. 4A, star symbol). These values were measured over "polysupercrystalline" films and contained resistivity contribution from grain boundary scattering.

Surface-ligand-dependent transport in Au NC solids has been of interest for studies of the transition between insulating and metallic behavior (*44*). For NC films with short organic ligands, an applied compression can induce electron delocalization (*45*). Au NC films with inorganic thiocyanate ligands also show metallic-type direct current resistivity (*46*). However, previously studied metallic NC solids shared the common trait that particles were rendered insoluble by the chemical or heat treatments that improve conductivity. This loss of solubility made it difficult to rule out partial sintering of NCs along the current percolation path.

Our SCs dissolved completely into their individual NC building blocks when placed into pure NMF or hydrazine (figs. S38 and S39). Dynamic light-scattering measurements (Fig. 4D) confirmed that the colloidal particles recovered from redissolved SCs after low-temperature electronic measurements were indeed individual Au NCs, so the metallic transport that we observed did not result from NC necking or sintering. We observed the metallic character of our assemblies with no thermal annealing and with infilling materials (glassy SnS_2 or $SnSe_2$) that did not have conduction bands aligned to the Fermi level of Au. Strong electronic coupling between neighboring NC units was achieved through a combination of the short interparticle distance and greater polarizability with a lower tunneling barrier afforded by the inorganic infill compared with that of analogous organic ligands.

REFERENCES AND NOTES

1. D. Vanmaekelbergh, *Nano Today* **6**, 419–437 (2011).
2. M. A. Boles, M. Engel, D. V. Talapin, *Chem. Rev.* **116**, 11220–11289 (2016).
3. C. B. Murray, C. R. Kagan, M. G. Bawendi, *Annu. Rev. Mater. Sci.* **30**, 545–610 (2000).
4. A. Fortini, E. Sanz, M. Dijkstra, *Phys. Rev. E Stat. Nonlin. Soft Matter Phys.* **78**, 041402 (2008).
5. E. V. Shevchenko, D. V. Talapin, N. A. Kotov, S. O'Brien, C. B. Murray, *Nature* **439**, 55–59 (2006).
6. M. A. Boles, D. V. Talapin, *J. Am. Chem. Soc.* **137**, 4494–4502 (2015).
7. T. Paik, B. T. Diroll, C. R. Kagan, C. B. Murray, *J. Am. Chem. Soc.* **137**, 6662–6669 (2015).
8. R. J. Macfarlane *et al.*, *Science* **334**, 204–208 (2011).
9. D. V. Talapin *et al.*, *Nature* **461**, 964–967 (2009).
10. X. Ye *et al.*, *Nat. Mater.* **16**, 214–219 (2017).
11. N. S. Mueller *et al.*, *Nature* **583**, 780–784 (2020).
12. J. Chen *et al.*, *Nano Lett.* **10**, 5103–5108 (2010).
13. J.-S. Lee, M. V. Kovalenko, J. Huang, D. S. Chung, D. V. Talapin, *Nat. Nanotechnol.* **6**, 348–352 (2011).
14. M. Y. Lin *et al.*, *Nature* **339**, 360–362 (1989).
15. G. H. Carey *et al.*, *MRS Commun.* **3**, 83–90 (2013).
16. M. P. Boneschanscher *et al.*, *Science* **344**, 1377–1380 (2014).
17. A. Abelson *et al.*, *Nat. Mater.* **19**, 49–55 (2020).
18. K. Whitham *et al.*, *Nat. Mater.* **15**, 557–563 (2016).

19. D. M. Balazs *et al*., *ACS Nano* **9**, 11951–11959 (2015).
20. M. C. Weidman, K. G. Yager, W. A. Tisdale, *Chem. Mater.* **27**, 474–482 (2015).
21. M. V. Kovalenko, M. Scheele, D. V. Talapin, *Science* **324**, 1417–1420 (2009).
22. A. E. Saunders, B. A. Korgel, *J. Phys. Chem. B* **108**, 16732–16738 (2004).
23. J. N. Israelachvili, *Intermolecular and Surface Forces* (Elsevier, 1985).
24. P. R. ten Wolde, D. Frenkel, *Science* **277**, 1975–1978 (1997).
25. T. K. Haxton, L. O. Hedges, S. Whitelam, *Soft Matter* **11**, 9307–9320 (2015).
26. M. G. Noro, D. Frenkel, *J. Chem. Phys.* **113**, 2941–2944 (2000).
27. N. Kallay, S. Žalac, *J. Colloid Interface Sci.* **253**, 70–76 (2002).
28. H. Liu, S. Garde, S. Kumar, *J. Chem. Phys.* **123**, 174505 (2005).
29. W. C. K. Poon *et al*., *Phys. Rev. Lett.* **83**, 1239–1242 (1999).
30. M. Muschol, F. Rosenberger, *J. Chem. Phys.* **107**, 1953–1962 (1997).
31. P. N. Pusey, W. van Megen, *Nature* **320**, 340–342 (1986).
32. D. Klotsa, R. L. Jack, *Soft Matter* **7**, 6294–6303 (2011).
33. T. Bian *et al*., *Nat. Chem.* **13**, 940–949 (2021).
34. J. W. Zwanikken, M. Olvera de la Cruz, *Proc. Natl. Acad. Sci. U.S.A.* **110**, 5301–5308 (2013).
35. Y. Jing, V. Jadhao, J. W. Zwanikken, M. Olvera de la Cruz, *J. Chem. Phys.* **143**, 194508 (2015).
36. R. M. Malossi, M. Girotto, A. P. Dos Santos, Y. Levin, *J. Chem. Phys.* **153**, 044121 (2020).
37. G. I. Guerrero García, M. Olvera de la Cruz, *J. Phys. Chem. B* **118**, 8854–8862 (2014).
38. O. Gliko *et al*., *J. Am. Chem. Soc.* **127**, 3433–3438 (2005).
39. A. Sauter *et al*., *Faraday Discuss.* **179**, 41–58 (2015).
40. J. Chelikowsky, *Quantum Theory of Real Materials* (Springer, 1996).
41. A. F. Clark, G. E. Childs, G. H. Wallace, *Cryogenics* **10**, 295–305 (1970).
42. J. Bardeen, *J. Appl. Phys.* **11**, 88–111 (1940).
43. C. Yamanouchi, K. Mizuguchi, W. Sasaki, *J. Phys. Soc. Jpn.* **22**, 859–864 (1967).
44. A. Zabet-Khosousi, A.-A. Dhirani, *Chem. Rev.* **108**, 4072–4124 (2008).
45. S. Henrichs, C. P. Collier, R. J. Saykally, Y. R. Shen, J. R. Heath, *J. Am. Chem. Soc.* **122**, 4077–4083 (2000).
46. J.-H. Choi *et al*., *Science* **352**, 205–208 (2016).
47. Y. Yu, D. Yu, B. Sadigh, C. A. Orme, *Nat. Commun.* **9**, 4211 (2018).
48. X. Lan *et al*., *Nat. Mater.* **19**, 323–329 (2020).

ACKNOWLEDGMENTS

We thank J. Ondry (University of Chicago) for many stimulating discussions and for critical reading of the manuscript. **Funding:** Self-assembly experiments, in situ x-ray scattering studies, and associated data interpretations were supported by the Office of Basic Energy Sciences (BES), US Department of Energy (DOE) (award no. DE-SC0019375). Nanomaterials synthesis and surface functionalization studies were supported by the Advanced Materials for Energy-Water Systems (AMEWS) Center, an Energy Frontier Research Center funded by the DOE, Office of Science, BES. Modeling and simulations of pair potentials were supported by the Midwest Integrated Center for Computational Materials (MICCoM) as part of the Computational Materials Sciences Program funded by the DOE, Office of Science, BES, Materials Sciences and Engineering Division (award no. 5J-30161-0010A). Spectroscopic and charge transport studies were supported by the Department of Defense Air Force Office of Scientific Research (grant no. FA9550-18-1-0099). D.H. and A.E. were supported by the Deutsche Forschungsgemeinschaft (award no. DFG1401/02). M.H. was supported by the University of Chicago Materials Research Science and Engineering Center, which is funded by the National Science Foundation (NSF) (award no. DMR-2011854). The work used resources of the Center for Nanoscale Materials, a U.S. DOE (DOE) Office of Science User Facility operated for the DOE Office of Science by Argonne National Laboratory (contract no. DE-AC02-06CH11357). Use of the Stanford Synchrotron Radiation Lightsource, SLAC National Accelerator Laboratory, is supported by the DOE, Office of Science, Office of Basic Energy Sciences (contract no. DE-AC02-76SF00515). C.P.N.T. was supported by the NSF (Graduate Research Fellowship no. DGE1106400). J.K.U. was supported by an Arnold O. Beckman Postdoctoral Fellowship in Chemical Sciences from the Arnold and Mabel Beckman Foundation. N.S.G. and D.V.T. were supported by an Alfred P. Sloan Research Fellowship, a David and Lucile Packard Foundation Fellowship for Science and Engineering, and a Camille and Henry Dreyfus Teacher-Scholar Awards. M.-O.C. thanks the Sherman Fairchild Foundation for computational support. **Author contributions:** I.C., E.M.J., and J.P. performed and designed the experiments, analyzed data, and cowrote the paper. D.H. participated in the early stage of the project under supervision by A.E. M.H.H., N.A.S., and A.M.H. synthesized nanocrystals and participated in data analysis; T.D.N. and A.D. performed simulations under supervision from M.-O.C. and D.T.L., respectively. J.K.U., S.W.T., and N.S.G. designed and performed beamtime synchrotron studies. D.V.T. conceived and designed experiments and simulations, analyzed data, cowrote the paper, and supervised the project. All authors discussed the results and commented on the manuscript. **Competing interests:** The authors declare no competing interests. **Data and materials availability:** All data needed to evaluate the conclusions in the study are present in the main text or the supplementary materials. Samples can be provided by the authors upon reasonable request under a materials transfer agreement with the university.

SUPPLEMENTARY MATERIALS

science.org/doi/10.1126/science.abm6753
Materials and Methods
Supplementary Text
Figs. S1 to S39
References (*49*–*82*)

5 October 2021; accepted 24 February 2022
10.1126/science.abm6753

Science

Self-assembly of nanocrystals into strongly electronically coupled all-inorganic supercrystals

Igor CoropceanuEric M. JankeJoshua PortnerDanny HauboldTrung Dac NguyenAvishek DasChristian P. N. TannerJames K. UtterbackSamuel W. Teitelbaum¸ Margaret H. HudsonNivedina A. SarmaAlex M. HinkleChristopher J. TassoneAlexander EychmüllerDavid T. LimmerMonica Olvera de la CruzNaomi S. GinsbergDmitri V. Talapin

Science, 375 (6587), • DOI: 10.1126/science.abm6753

Conducting colloidal nanocrystals

Organic capping ligands on nanocrystals can promote ordering of films and crystals but tend to block electronic conduction. Smaller inorganic ligands, such as diindium tetraselenide anions, promote conduction for semiconductors such as cadmium selenide but tend to form gels rather than crystals. Coropceanu *et al*. show that these inorganic anions can form electronically coupled crystals of nanocrystals of metals such as gold and nickel and semiconductors with high dielectric constants such as lead sulfide. In these cases, the multivalent anions bind in a dense but reversible manner to the nanocrystal surface and enable rearrangements that lead to the formation of crystals rather than amorphous gels. —PDS

Science (ISSN) is published by the American Association for the Advancement of Science. 1200 New York Avenue NW, Washington, DC 20005. The title *Science* is a registered trademark of AAAS.